

Noninvasive Quantitative Imaging of Selective Microstructure Sizes via Magnetic Resonance

Milena Capiglioni^{1,2,3}, Analia Zwick^{1,4,*}, Pablo Jiménez,^{1,2} and Gonzalo A. Álvarez^{1,2,4,†}

¹Centro Atómico Bariloche, CONICET, CNEA, S. C. de Bariloche 8400, Argentina

²Instituto Balseiro, CNEA, Universidad Nacional de Cuyo, S. C. de Bariloche 8400, Argentina

³Support Center for Advanced Neuroimaging (SCAN), Institute of Diagnostic and Interventional Neuroradiology, University of Bern, Bern 3010, Switzerland

⁴Instituto de Nanociencia y Nanotecnología, CNEA, CONICET, S. C. de Bariloche 8400, Argentina

(Received 31 July 2020; revised 21 October 2020; accepted 22 December 2020; published 25 January 2021)

Extracting quantitative microstructure information of living tissue by noninvasive imaging is an outstanding challenge for understanding disease mechanisms and allowing early stage diagnosis of pathologies. Magnetic resonance imaging (MRI) is a promising and widely used technique to pursue this goal, but still provides low resolution to reveal microstructure details. We here report on a method to produce images of filtered microstructure sizes based on selectively probing the nuclear-spin dephasing induced by the molecular diffusion within specific tissue compartments. The microstructure-size filter relies on suitable dynamical control of nuclear spins that sense magnetization “decay shifts” rather than the commonly used spin-echo decay rates. The feasibility and performance of the method are illustrated with proof-of-principle experiments and simulations on typical size distributions of white matter in the mouse brain. These results position spin-echo decay shifts as a promising MRI tool as they could offer the ability to perform noninvasive histology without assuming a microstructure distribution model. This sets a step towards unraveling diagnostic information based on microscopic parameters of biological tissue.

DOI: 10.1103/PhysRevApplied.15.014045

I. INTRODUCTION

Magnetic resonance imaging (MRI) has proven to be an excellent tool for acquiring noninvasive images, being applied on a daily basis for clinical diagnosis. However, the weak sensitivity for detecting nuclear spins inherent to biological tissues limits the spatial resolution of in-vivo MRI to hundreds of microns in preclinical scanners and to millimeters in clinical systems. This limitation imposes a challenge for existing methods to early detect diseases that produce changes at the cellular level [1–6]. Detecting these kind of pathologies in a development stage based on quantitative imaging will allow MRI to advance towards a new early diagnostic paradigm [4–10]. This is the aim of emerging quantum technologies such as quantum sensing for nanoscale imaging of biological tissues [11–15]. The current advances on controlling and extracting information from atoms, by employing quantum information and dynamical quantum control tools, may help to improve noninvasive MRI quantitative techniques of tissue microstructure [15–17].

Tissue microstructure information can be inferred by monitoring the dephasing of the nuclear spin precession of molecules inherent to biological tissues. The nuclear spins precess with the Larmor frequency determined by a strong magnetic field in MRI. The spin’s dephasing is induced by their molecular Brownian motion [7,18–20]. This molecular diffusion is restricted by tissue compartmentalization, and therefore its dynamics depends on microstructure properties such as cell sizes, density, and other morphological features that are orders of magnitude smaller than the size of an image voxel [21–26]. Diffusion-weighted MRI (DWI) exploits this property by employing a time-dependent magnetic field gradient to sense the microscopic motion of spins so that the precession frequency depends on their instantaneous position [16,20–22,27,28]. These dynamical control techniques are called modulated gradient spin-echo (MGSE) sequences [20,29] and are based on the Hahn spin-echo concept [30] and its generalization to multiple spin-echo sequences [31–33]. Such sequences refocus the phase accumulated by the spin’s precession by alternating the gradient sign. If the spins do not diffuse, the refocusing is perfect; however if they diffuse, the accumulated phase depends on the random motion of the spins and cannot be fully refocused. Therefore, the phase refocusing

* analia.zwick@cab.cnea.gov.ar

† gonzalo.alvarez@cab.cnea.gov.ar

leads to a spin echo whose decay contains information about the diffusion process.

Obtaining detailed microstructure information is challenging as the average spin signal contains information of multiple microstructure compartments that are orders of magnitude smaller than the measured voxel size [21–24,26]. The outstanding fundamental problems of DWI are the lack of specificity of the detected signal and reliable biophysical models to describe it. The inference of microstructure details is then indirect and the state-of-the-art approaches require the assumption of a microstructure-size distribution model [34,35]. Such inversions are notoriously very difficult because they are destabilized by the unavoidable effects of noise and imperfections of the model. Besides, this procedure requires acquiring several measurements to fit the characteristic parameters of the model and therefore demands long acquisition times that impose a challenge for in-vivo investigations [10,26,36–40].

We here report on a method to selectively filter the spin signal coming from specific microstructure sizes. The result of this filter are quantitative images based on a specific compartment-size-weighted contrast. DWI methods typically rely on characterizing the decay of the nuclear spin signal under MGSE sequences by its decay rate [19, 20]. Based on quantum information developments [41], nonuniform MGSE sequences were shown to have potential for monitoring molecular diffusion processes in tissue microstructure [16,17,42]. We implement these concepts on our approach, where the key conceptual change compared with state-of-the-art DWI methods is that quantitative information is encoded directly in the MRI signal as a “decay shift” rather than on a decay rate. We show that this can be exploited to selectively probe microstructure sizes without assuming a microstructure-size distribution model. We develop *size filters* based on the nonuniform oscillating gradient spin-echo (NOGSE) concept that contrast the signal generated by two spin-echo sequences [16,22]. Such sequence selectively probes the “decay shift” while factoring out the decay rate and other signal attenuation mechanisms induced by imperfections and T_2 -relaxation effects. We analytically and experimentally demonstrate the implementation of these microstructure-size filters, setting the bases for a mechanism for quantitative and precision imaging diagnostic tools.

II. MRI OF MOLECULAR DIFFUSION

The nuclear spins $S = \frac{1}{2}$ in molecules intrinsic to biological tissues, mainly from water’s protons, are typically observed on in-vivo MRI. The spins interact with the external uniform magnetic field $B_0\hat{z}$ of the magnet, and precess with the Larmor frequency γB_0 . A magnetic field gradient $G\hat{r}$ is applied along the direction \hat{r} for the spatial encoding. In a frame rotating at the Larmor frequency,

the spin’s precession frequency $\omega(t) = \gamma Gr(t)$ fluctuates, reflecting the random motion of the molecular diffusion process [19,20]. Here, $r(t)$ is the instantaneous position of the spin along the gradient direction and γ is the gyromagnetic ratio of the nucleus. The diffusion process induces the dephasing of the spin’s signal. By modulations of the gradient sign, the dephasing is partially refocused, forming the so-called spin echoes [30–33]. The spin-echo refocusing efficiency depends on how nuclear spins are scrambled by the diffusion process. If the motion of the molecules is restricted, e.g., due to compartmentalization of the tissue, the fluctuation amplitude of the precession frequency is limited and the dephasing rate is reduced.

During the diffusion weighted time T_E , the spins acquire a random phase $\phi(T_E)$ that typically follows a Gaussian distribution [43,44]. The magnetization in a voxel of the image becomes (Appendix A)

$$M(T_E) = e^{-\langle \phi^2(T_E) \rangle / 2} M(0). \quad (1)$$

The quadratic phase is averaged over the spin ensemble as [19–21,44]

$$\langle \phi^2(T_E) \rangle = \gamma^2 \int_0^{T_E} dt \int_0^{T_E} dt' G(t) G(t') \langle \Delta r(t - t') \Delta r(0) \rangle, \quad (2)$$

which is expressed in terms of the control applied to the system by $G(t)$ and the molecular displacement autocorrelation function $\langle \Delta r(0) \Delta r(t) \rangle$. Here $\Delta r(t) = r(t) - \langle r(t) \rangle$ is the instantaneous displacement of the spin position from its mean value [27,28]. Its autocorrelation function in a restricted media is $\langle \Delta r(0) \Delta r(t) \rangle = D_0 \sum_k b_k \tau_k e^{-|t|/\tau_k}$, where the coefficients b_k and correlation times τ_k depend on the geometry of the compartment, and D_0 is the free diffusion coefficient [21,45,46]. Usually, only one of these exponential functions is significant, and at least for planar, spherical, and cylindrical constraining geometries, this dominant first term will dominate the signal evolution [15, 16,21,22]. We consider this approximation for simplicity, and therefore we use $\langle \Delta r(0) \Delta r(t) \rangle = D_0 \tau_c e^{-|t|/\tau_c}$, where τ_c is the characteristic correlation time of the diffusion process [43]. The restriction length l_c of the microstructure compartment in which molecular diffusion is taking place is determined by the Einstein diffusion equation $l_c^2 = D_0 \tau_c$ [20]. The restriction length l_c and the geometric size of the compartment depend on its shape. For the example of cylinders oriented perpendicular to the direction of the magnetic field gradient, a good approximation is $l_c = 0.37d$, where d is the cylinder diameter [16,21,22,28]. Therefore, by monitoring the spin-echo decay by applying suitable control sequences, one can infer microstructure sizes [15,16,22–24,26,47]. The generalization of our results to the exact expression for the autocorrelation function is straightforward, as the solution for the quadratic

phase $\langle \phi^2(T_E) \rangle$ of Eq. (2) is a weighted sum of the solution discussed here for only one exponential term using the corresponding values for b_k and τ_k [21,45,46].

III. SPIN-ECHO DECAY SHIFT AS A PROBING-MICROSTRUCTURE PARADIGM

Two building block sequences for generating spin echoes at the evolution time T_E are shown in Figs. 1(a) and 1(b). An initial $\pi/2$ -excitation pulse is followed by a piecewise constant modulation as a function of time of the magnetic field gradient G . The modulation alternates the gradient's sign to produce refocusing periods. The sequence of Fig. 1(a) contains one ($N = 1$) refocusing period $t_H = T_E$ with a sign switch at $t_H/2$. This is a special case of the pulse gradient spin-echo sequence [18], providing a gradient modulation equivalent to a Hahn spin-echo sequence. This Hahn-like modulation was shown to be the most efficient DWI method for achieving micrometer-scale resolution [15]. In Fig. 1(b) we show N repetitive refocusing periods t_C , leading to a Carr-Purcell Meiboom-Gill (CPMG) or OGSE modulation [28,48] with a total time $Nt_C = T_E$. The spin-echo magnetization decay as a function of T_E/τ_c is reduced as the number of refocusing

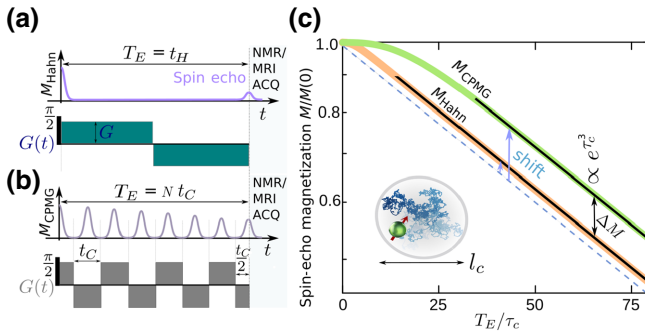


FIG. 1. Spin-echo decay shift as a paradigm for probing microstructure sizes. (a),(b) Magnetization decay under gradient spin-echo sequences. An initial $\pi/2$ -excitation pulse is followed by a piecewise constant magnetic field gradient that alternates its sign as a function of time. (a) A Hahn modulation contains one refocusing period of duration t_H and (b) a CPMG modulation contains N refocusing periods of duration t_C . After the total evolution time T_E of the gradient modulation, the signal is acquired using MRI acquisition (ACQ) encoding. (c) Normalized spin-echo decay $M(t)/M(0)$ (on a log scale) as a function of T_E/τ_c for Hahn (orange line) and CPMG ($N = 8$, green line) gradient modulations, with $\tau_c = 1.5$ ms and $G = 240$ mT/m. For $T_E/N \gg \tau_c$, both decaying signals have the same constant exponential decay rate proportional to τ_c^2 (black solid lines). The spin-echo decays differ by an exponential decay shift proportional to $\tau_c^3(1 + 2N)$ (marked with up arrows) with respect to the exponential decay $\exp(-\gamma^2 G^2 D_0 \tau_c^2 T_E)$ (dashed line). The decay shift is manifested in the contrast difference ΔM between both decays (double-headed arrow). The inset shows a scheme for molecules undergoing restricted Brownian motion within a compartment of restriction length $l_c = \sqrt{D_0 \tau_c}$.

periods N increases [31–33], as shown in Fig. 1(c). However, if the refocusing periods t_C and t_H are longer than the correlation time τ_c , the spins have been fully scrambled within the compartment, and the dephasing can no longer be refocused. This condition is called the *restricted diffusion* regime. Within this regime, the spin-echo decays as (see Appendix B) [16]

$$M(T_E)/M(0) \approx e^{-\gamma^2 G^2 D_0 \tau_c^2 [T_E - (1+2N)\tau_c]}, \quad (3)$$

leading to a decay rate $\frac{1}{2}[d\langle \phi^2(T_E) \rangle/dT_E] = \gamma^2 G^2 D_0 \tau_c^2$ independent of N [solid black lines in Fig. 1(c)]. Yet, the spin echo retains information of the transition from the free to the restricted diffusion regime. This information is manifested as a “decay shift” on the spin-echo decay signal of Eq. (3),

$$\gamma^2 G^2 D_0 \tau_c^3 (1 + 2N), \quad (4)$$

independent of the evolution time T_E , as shown in Fig. 1(c) with up arrows from the exponential decay $e^{-\gamma^2 G^2 D_0 \tau_c^2 T_E}$ (dashed line). Typically, the spin signal is only characterized by the decay rate [19,20]. Instead, the decay shift can be exploited to probe microstructure sizes [16,22,37] and we show here how it can be used to selectively filter microstructure sizes.

As this decay shift depends on N , it can be selectively probed by concatenating a Hahn with a CPMG gradient modulation by changing the ratio between their corresponding refocusing periods such that $T_E = (N - 1)t_C + t_H$ [Fig. 2(a)]. This control sequence conforms the NOGSE sequence [16,22], which also has the great advantage of factorizing out other relaxation mechanisms, allowing us

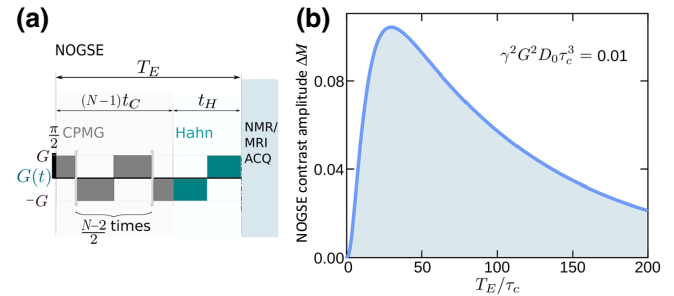


FIG. 2. NOGSE sequence and contrast. (a) The NOGSE sequence begins with an excitation $\pi/2$ -pulse followed by a modulated magnetic field gradient $G(t)$ resulting from concatenating the CPMG and Hahn sequences described in Fig. 1. NOGSE consists of N refocusing periods of gradient's sign modulations during the total evolution time T_E such that $T_E = (N - 1)t_C + t_H$, with Hahn and CPMG refocusing periods t_H and t_C , respectively. (b) NOGSE contrast ΔM as a function of T_E/τ_c for $G = 240$ mT/m and $N = 8$, with representative values of white-matter in the mouse brain $D_0 = 0.7 \mu\text{m}^2/\text{ms}$ and $\tau_c = 1.5$ ms.

to selectively probe the diffusion-induced decay. By keeping constant N and T_E , the effects of gradient switch errors and the unavoidable effects of the T_2 -relaxation time due to the intrinsic dephasing of the nuclear spins remain constant.

We define the NOGSE contrast as the amplitude ΔM given by the difference between the refocusing-period limits when $t_C = t_H$ (a CPMG modulation) and when $t_C \rightarrow 0$, $t_H \rightarrow T_E$ (a Hahn modulation). Within the restricted diffusion regime, this contrast amplitude is [see Fig. 1(c)]

$$\Delta M \approx e^{-\gamma^2 G^2 D_0 \tau_c^3 (T_E/\tau_c - 3)} (e^{\gamma^2 G^2 D_0 \tau_c^3 2(N-1)} - 1), \quad (5)$$

which is very sensitive to the restricted diffusion length l_c as it has a parametric dependence $l_c^6 \propto \tau_c^3$ provided by the spin-echo decay shift [16,22].

IV. NOGSE AS A SELECTIVE MICROSTRUCTURE-SIZE FILTER

The NOGSE contrast ΔM has a maximum as a function of the normalized echo time T_E/τ_c , as shown in Fig. 2(b). We exploit this maximum contrast to enhance the relative contribution to the signal from specific restriction lengths l_c from a given sample containing a size distribution. In order to perform a general analysis, we use the diffusion lengths

$$l_D = \sqrt{D_0 T_E}, \quad l_c = \sqrt{D_0 \tau_c}, \quad l_G = \sqrt[3]{\frac{D_0}{\gamma G}}, \quad (6)$$

where l_D is the length that a spin diffuses freely during the echo time T_E , l_c is the restriction length as defined above, and l_G is the characteristic diffusion length that produces a full dephasing by acquiring a phase of 2π [20,49,50]. Therefore, Eq. (5) can be parameterized in terms of the ratio between the diffusion length l_D and restriction length l_c , with respect to the full dephasing length l_G (see Appendix C), given by

$$L_D = \frac{l_D}{l_G} = (T_E \gamma^{2/3} G^{2/3} D_0^{1/3})^{1/2} \quad (7)$$

and

$$L_c = \frac{l_c}{l_G} = (\tau_c \gamma^{2/3} G^{2/3} D_0^{1/3})^{1/2}. \quad (8)$$

For the range of parameters where $L_D/L_c \gg 1$, $L_c^6 \ll 1$, and $L_D \gg 1$, the restricted diffusion regime is reached and the restriction diffusion length is small compared to the dephasing and diffusion lengths. Then, ΔM as a function of L_c can be approximated by a Gaussian function [see

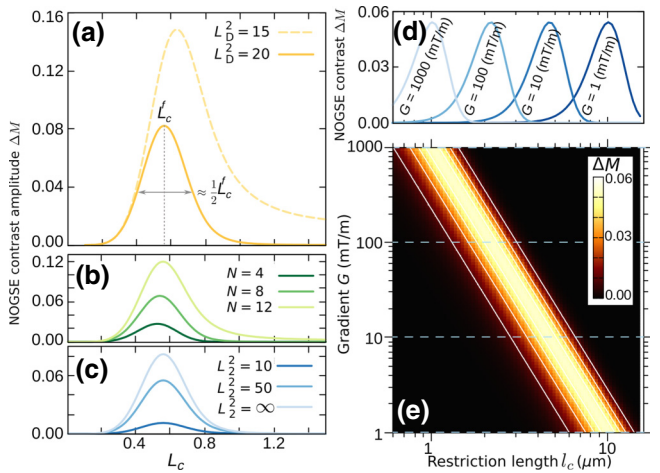


FIG. 3. Selective microstructure-size filter based on the NOGSE contrast. The NOGSE contrast amplitude ΔM as a function of L_c for different values of (a) L_D (with $N = 8$), (b) N (with $L_D^2 = 22$), and (c) L_2 (with $L_D^2 = 20$). In (a), ΔM shows a Gaussian filter functional dependence for $L_D \gg 1$ with a maximum at L_c^f . The filter's full width at half maximum is indicated with a gray double arrow. (d),(e) The NOGSE contrast amplitude ΔM as a function of the restriction length l_c and the gradient strength G , considering $N = 8$ and a constant value for $L_D^2 = 25$ by properly choosing T_E for each gradient. The considered dynamic range for the gradient strength G is achievable with current technologies. The horizontal dashed lines in (e) correspond to the specific cases plotted in (d). Here $D_0 = 0.7 \mu\text{m}^2/\text{ms}$.

Fig. 3(a) and Appendix D],

$$\Delta M \approx 2(N-1)e^{-3/2}(L_c^f)^6 \exp \left[-12 \left(\frac{L_c - L_c^f}{L_c^f} \right)^2 \right]. \quad (9)$$

The NOGSE contrast therefore acts as a microstructure-size “bandpass” filter with L_c^f as the filter-center size, i.e., the size where the contrast has its maximum,

$$L_c^f \approx (3/2)^{1/4} L_D^{-1/2}. \quad (10)$$

The filter-band selectivity is defined by the ratio between the full width at half maximum (FWHM) and L_c^f , $\text{FWHM}/L_c^f \approx \sqrt{(\ln 2)/3} \approx 0.5$.

The maximum of ΔM at the size L_c^f can be tuned to highlight a given restriction length l_c by properly choosing the sequence control parameters, i.e., the gradient strength G and the evolution time T_E (see Fig. 3).

The filtered size L_c^f decreases as the control parameter L_D increases according to Eq. (10). However, increasing L_D decreases the contrast amplitude which is proportional to $(L_c^f)^6 \propto 1/L_D^3$ according to Eqs. (9)–(10); see Fig. 3(a). Therefore, the minimum size that can be filtered in practice is limited by the signal-to-noise ratio (SNR) and the maximum achievable gradient strength as $L_D \propto \sqrt[3]{G}$

according to Eq. (7). This decrease in ΔM can be compensated linearly by increasing the number of refocusing periods N , as long as $L_D^2/L_c^2N = T_E/\tau_c N \gg 1$ in order to hold the restricted diffusion regime [see Eq. (9) and Fig. 3(b)].

A practical limitation is imposed by the unavoidable T_2 -relaxation effects that add an extra signal decay to the NOGSE contrast

$$\Delta M_{T_2} = \Delta M e^{-L_D^2/L_2^2}, \quad (11)$$

where $L_2 = l_2/l_G$ and $l_2 = (D_0 T_2)^{1/2}$. The contrast attenuation due to the T_2 -relaxation effect is shown in Fig. 3(c) for different values of L_2^2 . Remarkably, the filter shape and center remain the same as the case in which $T_2 \rightarrow \infty$.

Our results show that one can produce *quantitative images* based on a signal contrast generated only by specific microstructure sizes and without assuming a size distribution model. The method avoids extracting the microstructure size by fitting a size distribution model, which is time consuming as it typically requires several measurements [8,26,36,37,47,51]. Instead, using our approach, selective microstructure-size information can be extracted from a single value of the contrast for each voxel, requiring only two image acquisitions.

The filter amplitude ΔM and “bandwidth” in Eq. (9) remain constant by varying the gradient strength and the evolution time, keeping fixed the parameter L_D , as shown in Fig. 3(d). Therefore, one can use this tool to scan a restriction-size distribution while keeping constant the filtering properties. Note that, while this scanning tool requires a comparable number of measurements and acquisition time with respect to state-of-the-art approaches, the strength of our method is that it does not need the assumption of a size distribution model. We show in Fig. 3(e) the dynamic range of restriction lengths that can be scanned, assuming a diffusion coefficient typical of white matter in the mouse brain, and considering the range of gradient strengths achievable with current technologies.

V. SELECTIVE SIZE FILTERING IN TYPICAL MICROSTRUCTURE-SIZE DISTRIBUTIONS

We perform proof-of-principle simulations to show the NOGSE contrast filter’s performance when applied to microstructure-size distributions inherent to heterogeneous biological tissues; see Fig. 4. Typical size distributions $P(l_c)$ are bimodal and log-normal functions [4,36,37,52,53], as shown in Figs. 4(a) and 4(b). The NOGSE contrast for a size distribution is determined by

$$\Delta M = \int_{l_c} P(l_c) \Delta M(l_c) dl_c, \quad (12)$$

where $\Delta M(l_c)$ is the contrast contribution for a given restriction length l_c . In Figs. 4(c) and 4(d) we show the predicted ΔM as a function of $l_c^f = L_c^f l_G$, where G and T_E are

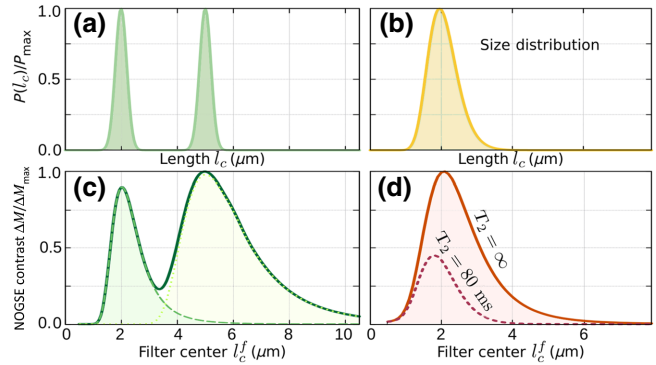


FIG. 4. Selective size filtering with NOGSE contrast of typical microstructure-size distributions. Size distribution probability $P(l_c)$ for two typical cases of tissue microstructure: (a) a bimodal Gaussian distribution with means $l_c = 2$ and $5 \mu\text{m}$, and standard deviation $0.2 \mu\text{m}$ for both peaks; and (b) a log-normal distribution with median $2 \mu\text{m}$ and standard deviation $1.22 \mu\text{m}$, representative of white-matter size distributions. (c),(d) Normalized NOGSE contrast amplitude ΔM as a function of the filter center l_c^f . The diffusion coefficient is $D_0 = 0.7 \mu\text{m}^2/\text{ms}$ in both cases. (c) The dashed lines show ΔM obtained by separately considering each of the components of the bimodal distribution of panel (a). The low overlap between the dashed lines demonstrates the filtering property of the NOGSE contrast. Here $L_D^2 = 25$, $N = 8$, and $\Delta M_{\max} = 0.027$. (d) Normalized NOGSE contrast amplitude ΔM for the case including transversal T_2 -relaxation effects ($T_2 = 80 \text{ ms}$; dashed line) is contrasted with the ideal case without relaxation effects ($T_2 = \infty$; solid line) for the distribution of panel (b). Here $L_D^2 = 11$, $N = 4$, and $\Delta M_{\max} = 0.08$.

changed simultaneously keeping L_D constant. The center of the filter at l_c^f is therefore swept while the filter amplitude $\Delta M(l_c^f)$ is kept constant. The resulting filtered signal as a function of the filter center l_c^f resembles the original size distributions, where the log-normal peak and both Gaussian peaks are clearly identified. To further demonstrate the filter selectivity, in Fig. 4(c) we also show the result of applying the filter if only one of the Gaussians is present at the time, proving that if one chooses l_c^f equal to the center of one of the two Gaussian distributions, the other component is filtered out.

These simulations demonstrate two of our main results: one can apply the NOGSE contrast filter to produce quantitative images with a weighted contrast based on the probability of finding a specific restriction length, and one can exploit this filtering tool to scan a size distribution without assuming a model for $P(l_c)$.

The effect of T_2 relaxation is shown in Fig. 4(d) for typical values of white-matter tissue in a mouse, demonstrating the limitation it imposes by attenuating the signal-to-noise ratio. The transversal T_2 -relaxation limits the largest microstructure size that can be filtered, as the restricted diffusion regime has to be achieved. A good SNR for ΔM is only obtained for $L_c < L_D < L_2$. For short T_2 , the

strategy is therefore to use the lowest possible value of L_D and reduce the number of refocusing periods N so as to remain in the restricted regime. Then, a size-filter sweep can be done by varying only the gradient amplitude while keeping $T_E \lesssim T_2$ constant. In this way, the filter amplitude $\Delta M(l_c)$ varies, but this approach allows us to mitigate the signal loss induced by intrinsic relaxation effects.

We implement the microstructure-size filter method on an ex-vivo mouse brain focusing on the corpus callosum (CC) region (see experimental details in Appendices E–F). We consider the CC region since it contains aligned axons and is a paradigmatic model for log-normal size distributions [4,36,37,52,53]. In Fig. 5(a) we show image maps of ΔM for two gradient strengths. The largest gradient acts as a “bandpass” Gaussian filter of the lower microscropic sizes of the distribution, compared to the weaker gradient that acts as a “high-pass” filter of the larger sizes. Therefore, Fig. 5(a) clearly highlights well-known zones (e.g., splenium and isthmus) of the CC with complementary colors depending of the microstructure sizes they contain. Several studies have shown that the splenium has smaller axon diameters than those in the isthmus region

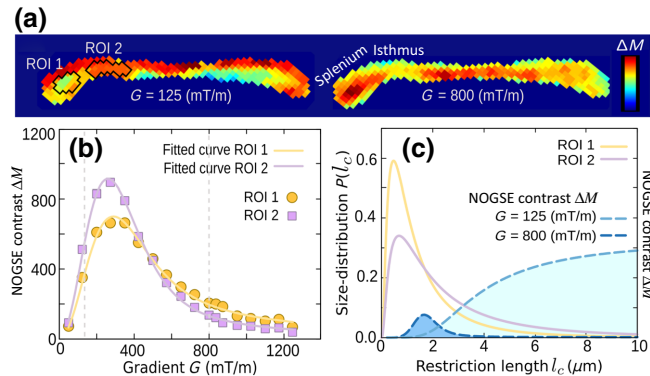


FIG. 5. Noninvasive NOGSE imaging of selective microstructure sizes in an ex-vivo mouse brain. (a) Two images based on the NOGSE contrast of the corpus callosum region of a mouse brain for two gradient strengths. The color scale covers the full range of contrast signals in each image. Two regions of interest in the splenium (ROI 1) and isthmus (ROI 2) are indicated with black contours. Each image is acquired for $N = 2$ and $T_E = 21.5$ ms with resolution $78 \times 78 \mu\text{m}^2$ and an acquisition time of approximately 17 min (see Appendix F). (b) Average NOGSE contrast signal (symbols) as a function of the gradient strength G for the two regions of interest. The vertical dashed lines mark the gradient strengths used in (a). The solid lines are fits to the experimental data of our theoretical model following Eq. (12) for a log-normal distribution. The fitted parameters are the medians 1.08 ± 0.06 and $1.87 \pm 0.04 \mu\text{m}$ and the geometric standard deviations 2.58 ± 0.03 and $2.91 \pm 0.04 \mu\text{m}$ for ROI 1 and 2, respectively. We considered a uniform $D_0 = 0.7 \mu\text{m}^2/\text{ms}$ as a representative diffusion coefficient to fit the size distribution. (c) Size distributions (solid lines) that best fit the experimental data for the selected regions of interest. The dashed lines show $\Delta M(l_c)$ predicted by our model for the two gradients used in (a).

[37,40,54,55]. Consistently, the NOGSE contrast filter in the splenium region with smaller microstructure sizes for the larger gradient $G = 800 \text{ mT/m}$, and the isthmus region with the larger microstructures sizes for the lower gradient $G = 125 \text{ mT/m}$. These images then set a contrast that directly encodes microstructure-size information with the probability of finding a specific restriction size in each pixel, setting a proof of principle of our method.

To further demonstrate this claim and therefore give insights into the usefulness of the NOGSE contrast filter, we acquire images for multiple values of the gradient strengths ranging from 125 to 1250 mT/m. The resulting behavior of the filter is demonstrated quantitatively in Figs. 5(b) and 5(c) for two regions of interest in the splenium and isthmus regions. The average ΔM as a function of the gradient for the regions of interest is shown with symbols in Fig. 5(b). As it is not the purpose of this work to validate the size distribution models of the CC regions, but only to demonstrate the selective microstructure-size performance of our method, we assume an established log-normal distribution model according to previous works [37,40,54,55]. We then fit the experimental curves with our theoretical prediction following Eq. (12) (see Appendix G). In Fig. 5(c) we show the reconstructed distributions for the regions of interest and the $\Delta M(l_c)$ filter for the two gradient strengths used in panel (a). The overlap between $P(l_c)$ and $\Delta M(l_c)$ is consistent with the signal contrast shown in Fig. 5(a): region of interest (ROI) 1 has smaller sizes than ROI 2, and therefore ROI 1 has higher ΔM for $G = 800 \text{ mT/m}$; conversely, ROI 2 has higher contrast amplitude for $G = 125 \text{ mT/m}$.

The excellent agreement between the model and the experimental data as shown in Fig. 5(b) fully demonstrates the reliability of the quantitative images shown in Fig. 5(a) based on the NOGSE contrast microstructure-size filter and the assumed log-normal model.

VI. CONCLUSIONS

We introduce a method for noninvasive quantitative imaging of selective microstructure sizes based on probing nuclear-spin dephasing induced by molecular diffusion with magnetic resonance. Conversely to standard diffusion-weighted imaging approaches that are based on observing the decay rate of the spin signal, we exploit dynamical control tools using nonuniform oscillating gradients to selectively probe a decay shift on spin-echo decays. This decay shift contains quantitative information of microstructure sizes that restrict the molecular diffusion. We generate a contrast amplitude that behaves as a microstructure-size filter to selectively probe a specific restriction length determined by the control parameters. We show the feasibility and performance of the method with proof-of-principle simulations and experiments on typical size distributions of white-matter tracts in a mouse

brain. Quantitative images based on a weighted contrast determined by the probability of finding specific diffusion restriction lengths are extracted from only two images. This is an alternative to extracting quantitative microstructure information while significantly reducing the tens of images that typically demand the inference of microstructure sizes from data fittings [8,26,36,37,47,51]. Even though intrinsic T_2 relaxation may represent a limitation, the filter shows excellent performance probing quantitative information of microstructure details on biological tissue as in the white matter of a mouse brain. We are able to filter sizes between approximately $0.1 - 10 \mu\text{m}$, which is a range much lower than the present image resolution. This work lays the foundations of a conceptual tool with low overhead for designing quantitative methods for noninvasive imaging of tissue microstructure. An important application of this tool is that it can allow scanning a size distribution without the need of assuming a size distribution model. This diagnostic tool opens up an avenue to explore for in-vivo imaging. Further studies will be focused on optimizing the control parameters to optimize the measurement time and information gain, and on validating quantitatively the method with properly designed phantoms where size distributions can be known exactly. Then it is important to explore potential applications where images based on selective microstructure sizes could be useful. In addition, these results can also be applied for characterizing material microstructures, such as in rocks that are of particular interest for oil extraction, and for nanoscale imaging of biological tissues with quantum sensors based on noise spectroscopy [11–13].

ACKNOWLEDGMENTS

We acknowledge Soledad Esposito, Veronica Piatti, and Micaela Kortsarz for preparing the ex-vivo mouse

brain, and Federico Turco for scripting assistance to process the experimental data. We thank Lucio Frydman and Jorge Jovicich for fruitful discussions. This work is supported by CNEA, ANPCyT-FONCyT PICT-2017-3447, PICT-2017-3699, PICT-2018-04333, PIP-CONICET (11220170100486CO), UNCUYO SIIP Tipo I 2019-C028, Instituto Balseiro. A.Z. and G.A.A. are members of the Research Career of CONICET. M.C. acknowledges support from a CONICET fellowship. M.C. and P.J. acknowledge support from Instituto Balseiro fellowships.

APPENDIX A: MAGNETIZATION DECAY OF A SPIN ENSEMBLE UNDER DYNAMICAL CONTROL

The magnetization signal observed from an ensemble of noninteracting and equivalent spins, under the effect of dynamical control, is $M(t) = \langle e^{-i\phi(t)} \rangle M(0)$. Here, $\phi(t) = \int_0^t \omega(t)dt$ is the phase acquired by a spin during the evolution time t , and the brackets denote the average over the random phases of the spin ensemble [30,31]. For the considered dynamical control with modulated gradient spin-echo sequences, the average phase becomes null, $\langle \phi(t) \rangle = 0$. Then, as $\phi(t)$ typically follows a Gaussian distribution [44], the signal will depend on the random phase variance $M(t) = e^{-\langle \phi^2(t) \rangle / 2} M(0)$.

The variance expressed in terms of the control applied to the system by $G(t)$ and the molecular displacement autocorrelation function $\langle \Delta r(0) \Delta r(t) \rangle = D_0 \tau_c e^{-|t|/\tau_c}$ [16, 21,22] are given in Eq. (2) of the main text.

For a piecewise constant modulation $G(t)$ that switches its sign N times at times t_i with $i = 0, \dots, N - 1$ during the evolution time T_E , the quadratic phase of the magnetization decay is

$$\begin{aligned} \langle \phi^2(T_E) \rangle &= \gamma^2 G^2 D_0^2 \tau_c \sum_{i=0}^{N-1} \sum_{j=0}^{N-1} \int_{t_i}^{t_{i+1}} \int_{t_j}^{t_{j+1}} e^{-|t-t'|/\tau_c} (-1)^i (-1)^j dt' dt \\ &= \gamma^2 G^2 D_0^2 \tau_c \sum_{i=0}^{N-1} \sum_{j=0}^{N-1} (-1)^i (-1)^j \left[\left(\begin{array}{ll} \left\{ 2\tau_c t_j - \tau_c^2 e^{-(t_i-t_j)/\tau_c}, & t_j \leq t_i \\ -\tau_c^2 e^{-(t_i-t_j)/\tau_c}, & t_i < t_j \end{array} \right. \right) \right. \\ &\quad + \left(\begin{array}{ll} \left\{ 2\tau_c t_{j+1} - \tau_c^2 e^{-(t_{i+1}-t_{j+1})/\tau_c}, & t_{j+1} \leq t_{i+1} \\ -\tau_c^2 e^{-(t_{i+1}-t_{j+1})/\tau_c} + 2\tau_c t_{i+1}, & t_{i+1} < t_{j+1} \end{array} \right. \right) \\ &\quad - \left(\begin{array}{ll} \left\{ 2\tau_c t_j - \tau_c^2 e^{-(t_{i+1}-t_j)/\tau_c}, & t_j \leq t_{i+1} \\ -\tau_c^2 e^{-(t_{i+1}-t_j)/\tau_c} + 2\tau_c t_{i+1}, & t_{i+1} < t_j \end{array} \right. \right) \\ &\quad \left. \left. - \left(\begin{array}{ll} \left\{ 2\tau_c t_{j+1} - \tau_c^2 e^{-(t_i-t_{j+1})/\tau_c}, & t_{j+1} \leq t_i \\ -\tau_c^2 e^{-(t_i-t_{j+1})/\tau_c} + 2\tau_c t_i, & t_i < t_{j+1} \end{array} \right. \right) \right] \right]. \end{aligned} \quad (\text{A1})$$

APPENDIX B: MAGNETIZATION DECAY WITHIN THE RESTRICTED DIFFUSION REGIME

In the restricted diffusion regime all terms are proportional to $e^{-|t_i-t_j|/\tau_c} \rightarrow 0$ as $|t_i - t_j| \gg \tau_c$ for all $i \neq j$; therefore, the non-null terms in Eq. (A1) are those with $i = j$. The phase variance is then

$$\begin{aligned} -\frac{1}{2}\langle\phi^2(T_E)\rangle &= -\frac{1}{2}\gamma^2G^2D_0^2\tau_c \sum_{i=0}^{N-1} \sum_{j=0}^{N-1} (-1)^i(-1)^j [(2\tau_ct_j - \tau_c^2e^{-(t_i-t_j)/\tau_c})\delta_{ij} \\ &\quad + (2\tau_ct_{j+1} - \tau_c^2e^{-(t_{i+1}-t_{j+1})/\tau_c})\delta_{i+1,j+1} \\ &\quad - (2\tau_ct_j - \tau_c^2e^{-(t_{i+1}-t_j)/\tau_c})\delta_{i+1,j} \\ &\quad - (2\tau_ct_{j+1} - \tau_c^2e^{-(t_i-t_{j+1})/\tau_c})\delta_{ij+1}] \\ &= -\frac{1}{2}\gamma^2G^2D_0^2\tau_c \left[2\tau_c \sum_{i=1}^N (t_i - t_{i-1}) - \tau_c^2(4N + 2) \right] \\ &= -\gamma^2G^2D_0^2\tau_c^2[T_E - (2N + 1)\tau_c]. \end{aligned} \quad (\text{B1})$$

Then, the *decay rate* is $d\langle\phi^2(T_E)\rangle/dT_E = \gamma^2G^2D_0^2\tau_c^2$, and the *decay shift* is the time-independent term $\gamma^2G^2D_0^2\tau_c^3(2N + 1)$, which can also be derived from

$$\begin{aligned} \gamma^2G^2D_0\tau_c^3(2N + 1) \\ = \gamma^2G^2D_0\tau_c(2N + 1) \int_0^\infty dt t\langle\Delta r(0)\Delta r(t)\rangle. \end{aligned} \quad (\text{B2})$$

APPENDIX C: NOGSE CONTRAST AMPLITUDE

One can obtain an analytical expression for the magnetization decay in Eq. (A1) for the Hahn, CPMG, and NOGSE spin-echo sequences described in Figs. 1 and 2 of the main text. In the restricted diffusion regime $T_E, t_H, t_C \gg \tau_c$, we have

$$M_{\text{Hahn}}(t_H) = \exp \left\{ -\gamma^2G^2D_0\tau_c^3 \left[\frac{t_H}{\tau_c} - 3 \right] \right\}, \quad (\text{C1a})$$

$$M_{\text{CPMG}}(Nt_C, N) = \exp \left\{ -\gamma^2G^2D_0\tau_c^3 \left[\frac{Nt_C}{\tau_c} - (2N + 1) \right] \right\}, \quad (\text{C1b})$$

$$M_{\text{NOGSE}}(T_E, N, t_C) = \exp \left\{ -\gamma^2G^2D_0\tau_c^3 \left[\frac{T_E}{\tau_c} - (2N + 1) \right] \right\}, \quad (\text{C1c})$$

with $T_E = (N - 1)t_C + t_H$.

We define the NOGSE contrast amplitude ΔM as the difference between $M_{\text{NOGSE}}(T_E, N, t_C = t_H) =$

$M_{\text{CPMG}}(T_E/N, N)$ and $M_{\text{NOGSE}}(T_E, N, t_C \rightarrow 0) \simeq M_{\text{Hahn}}(T_E)$, i.e.,

$$\Delta M(T_E, N) = M_{\text{CPMG}}(T_E, N) - M_{\text{Hahn}}(T_E). \quad (\text{C2})$$

Then, we obtain Eq. (5) by substituting Eqs. (C1a) and (C1b) into Eq. (C2):

$$\Delta M \approx e^{-\gamma^2G^2D_0\tau_c^3(T_E/\tau_c - 3)}(e^{\gamma^2G^2D_0\tau_c^32(N-1)} - 1). \quad (\text{C3})$$

This NOGSE contrast, using the dimensionless variables L_D, L_c defined in the main text, yields

$$\Delta M(L_D, L_c, N) = e^{-L_c^4(L_D^2 - 3L_c^2)}(e^{2(N-1)L_c^6} - 1). \quad (\text{C4})$$

The general expression for ΔM that includes all diffusion time scales can be obtained from Eq. (A1) by replacing the time intervals as defined in Fig. 2(a) of the main text.

APPENDIX D: GAUSSIAN MICROSTRUCTURE-SIZE FILTER DERIVATION

The NOGSE contrast amplitude in the restricted diffusion regime, Eq. (C4), can be approximated by

$$\Delta M \approx e^{-L_c^4(L_D^2 - 3L_c^2)}2(N - 1)L_c^6 \quad (\text{D1})$$

for $L_c \ll 1$. The maximum of ΔM occurs at $d\Delta M/dL_c = 0$. In the asymptotic limit of $L_D \gg 1$, it is achieved for

$$L_c = L_c^f \approx (3/2)^{1/4} L_D^{-1/2} + \mathcal{O}(L_D^{-7/2}), \quad (\text{D2})$$

where L_c^f is the center of the filter as described in Eq. (10).

The NOGSE contrast amplitude can be approximated by a Taylor expansion about L_c at $L_c \approx L_c^f$ of the expression given in Eq. (D1),

$$\Delta M \approx e^{-3/2} 3 \sqrt{\frac{3}{2}} (N-1) L_D^{-3} - 36e^{-3/2} (N-1) L_D^{-2} \times (L_c - L_c^f)^2 + \mathcal{O}[(L_c - L_c^f)^4]. \quad (\text{D3})$$

We use this expansion to define the first moments of the Gaussian filter function of Eq. (9), obtaining

$$\Delta M \approx 2(N-1)e^{-3/2}(L_c^f)^6 \exp\left[-12\left(\frac{L_c - L_c^f}{L_c^f}\right)^2\right]. \quad (\text{D4})$$

This expression is then verified to approximate very well the exact expression derived from Eq. (A1) within the regime of $L_D \gg 1$ and $L_c \ll 1$.

APPENDIX E: EX-VIVO MOUSE BRAIN PREPARATION

The experiments were approved by the Institutional Animal Care and Use Committee of the Comisión Nacional de Energía Atómica under protocol number 08_2018. One mouse was sacrificed and its brain was fixed in 4% formaldehyde, dehydrated and equilibrated in 30% sucrose. Previous to the MRI experiments, the brain was washed twice with PBS prior to the insertion into a 15 ml falcon tube filled with PBS. The brain was left in the magnet for at least three hours prior to the reported experiments to reach thermal equilibration.

APPENDIX F: MRI EXPERIMENTS

The experiments are performed on a 9.4T Bruker Avance III HD WB NMR spectrometer with a 1H resonance frequency of $\omega_z = 400.15$ MHz. We use a Micro 2.5 probe capable of producing gradients up to 1500 mT/m in three spatial directions. The experimental temperature is stabilized at 21 °C. We programme and implement with Paravision 6 the NOGSE MRI sequence shown in Fig. 6. The sequence parameters are as follows: repetition time 2000 ms, $T_{\text{echo time}} = 55$ ms, FOV = 15 × 15 mm² with a matrix size of 192 × 192, leading to an in-plane resolution of 78 × 78 μm², and a slice thickness of 1 mm with 128 signal averages. The two images are obtained with echo planar imaging (EPI) encoding with four segments (image acquisition time approximately 17 min) and then subtracted to generate ΔM . The NOGSE modulation time is $T_E = 21.5$ ms with $N = 2$. The NOGSE gradients are applied perpendicular to the main axis of the axons in the corpus callosum. The NOGSE contrast ΔM is determined from an image generated with $t_H = t_C = 10.75$ ms for the

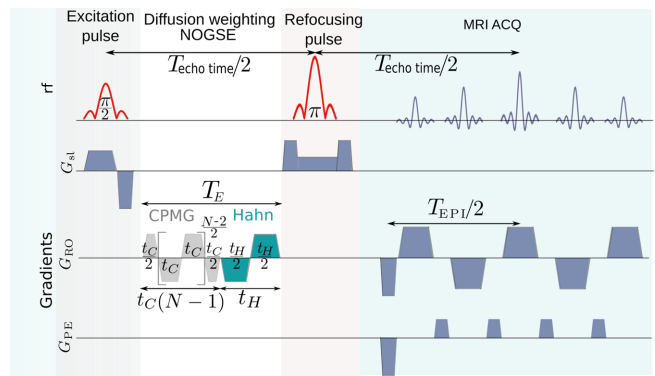


FIG. 6. Scheme for the experimental implementation of the NOGSE sequence. An initial selective rf excitation $\pi/2$ pulse is applied to select a tissue slice. It is followed by a NOGSE gradient modulation of duration T_E , following the scheme described in Fig. 2(a) of the main text. During the evolution time T_E , the gradient strength and sign are modulated with trapezoidal shapes. Then a selective rf π pulse is applied to refocus magnetic field inhomogeneities. At the end a spatial EPI encoding is applied for acquiring an image. Three gradients are applied in the three spatial directions for slide selection G_{SL} , for read orientation G_{RO} , and phase encoding G_{PE} . The NOGSE gradients can be applied in arbitrary orientations.

CPMG modulation and with $t_H = 0.5$ ms and $t_C = 21$ ms for the Hahn modulation. The set of parameter values are chosen so as to achieve a good SNR for performing proof-of-principle experiments. Further studies should be considered to explore the optimal values for acquiring the images in the shortest possible time.

APPENDIX G: EXPERIMENTAL DATA ANALYSIS

The average signal is analyzed from the pixels in the regions of interest of Fig. 5(a) of the main text, and plotted as a function of G in Fig. 5(b). Fittings to the theoretical model are done assuming a uniform $D_0 = 0.7 \mu\text{m}^2/\text{ms}$ and a log-normal distribution $P(l_c) = (1/\sqrt{2\pi}\sigma l_c)e^{-(\ln(l_c)-\mu)^2/2\sigma^2}$ with median e^μ and geometric standard deviation e^σ . This implies that no extra assumptions are considered for the tissue model (e.g., intra- and extra-cellular compartments). Therefore, a single log-normal distribution is thus fitted to the experimental data, regardless of the potential of additional heterogeneity. This means that all underlying compartments (e.g., extracellular, intracellular, etc.) reflected in the diffusion-weighted signal are assumed to be described by a single log-normal distribution. We consider a distribution of restriction lengths l_c without assuming particular geometries. Remarkably, the excellent agreement of the fitted curves to the experimental data in Fig. 5(b) of the main text is consistent with these simple assumptions.

- [1] S. G. Waxman and M. V. L. Bennett, Relative conduction velocities of small myelinated and non-myelinated fibres in the central nervous system, *Nat. New Biol.* **238**, 217 (1972).
- [2] A. R. Padhani, G. Liu, D. M. Koh, T. L. Chenevert, H. C. Thoeny, T. Takahara, A. Dzik-Jurasz, B. D. Ross, M. Van Cauteren, D. Collins, D. A. Hammoud, G. J. S. Rustin, B. Taouli, and P. L. Choyke, Diffusion-weighted magnetic resonance imaging as a cancer biomarker: Consensus and recommendations, *Neoplasia* **11**, 102 (2009).
- [3] V. Drago, C. Babiloni, D. Bartrés-Faz, A. Caroli, B. Bosch, T. Hensch, M. Didic, H.-W. Klafki, M. Pievani, J. Jovicich, L. Venturi, P. Spitzer, F. Vecchio, P. Schoenknecht, J. Wiltfang, A. Redolfi, G. Forloni, O. Blin, E. Irving, C. Davis, H.-g. Hårdemark, and G. B. Frisoni, Disease tracking markers for alzheimer's Disease at the prodromal (MCI) stage, *J. Alzheimers Dis.* **26**, 159 (2011).
- [4] N. S. White, T. B. Leergaard, H. D'Arceuil, J. G. Bjaalie, and A. M. Dale, Probing tissue microstructure with restriction spectrum imaging: Histological and theoretical validation, *Hum. Brain Mapp.* **34**, 327 (2013).
- [5] N. S. White, C. R. McDonald, N. Farid, J. Kuperman, D. Karow, N. M. Schenker-Ahmed, H. Bartsch, R. Rakow-Penner, D. Holland, A. Shabaik, A. Bjørnerud, T. Hope, J. Hattangadi-Gluth, M. Liss, J. K. Parsons, C. C. Chen, S. Raman, D. Margolis, R. E. Reiter, L. Marks, S. Kesari, A. J. Mundt, C. J. Kaine, B. S. Carter, W. G. Bradley, and A. M. Dale, Diffusion-weighted imaging in cancer: Physical foundations and applications of restriction spectrum imaging, *Cancer Res.* **74**, 4638 (2014).
- [6] C. Enzinger, F. Barkhof, O. Ciccarelli, M. Filippi, L. Kappos, M. A. Rocca, S. Ropele, À. Rovira, T. Schneider, N. de Stefano, H. Vrenken, C. Wheeler-Kingshott, J. Wuerfel, F. Fazekas and MAGNIMS study group, Nonconventional MRI and microstructural cerebral changes in multiple sclerosis, *Nat. Rev. Neurol.* **11**, 676 (2015).
- [7] D. Le Bihan, Looking into the functional architecture of the brain with diffusion MRI, *Nat. Rev. Neurosci.* **4**, 469 (2003).
- [8] J. Xu, H. Li, K. D. Harkins, X. Jiang, J. Xie, H. Kang, M. D. Does, and J. C. Gore, Mapping mean axon diameter and axonal volume fraction by MRI using temporal diffusion spectroscopy, *Neuroimage* **103**, 10 (2014).
- [9] F. Grussu, T. Schneider, C. Tur, R. L. Yates, M. Tachroud, A. Ianuș, M. C. Yiannakas, J. Newcombe, H. Zhang, D. C. Alexander, G. C. DeLuca, and C. A. M. Gandini Wheeler-Kingshott, Neurite dispersion: A new marker of multiple sclerosis spinal cord pathology? *Ann. Clin. Transl. Neurol.* **4**, 663 (2017).
- [10] D. C. Alexander, T. B. Dyrby, M. Nilsson, and H. Zhang, Imaging brain microstructure with diffusion mri: Practicality and applications, *NMR Biomed.* **32**, e3841 (2019).
- [11] T. Staudacher, N. Raatz, S. Pezzagna, J. Meijer, F. Reinhard, C. A. Meriles, and J. Wrachtrup, Probing molecular dynamics at the nanoscale via an individual paramagnetic centre, *Nat. Commun.* **6**, 8527 (2015).
- [12] J. F. Barry, M. J. Turner, J. M. Schloss, D. R. Glenn, Y. Song, M. D. Lukin, H. Park, and R. L. Walsworth, Optical magnetic detection of single-neuron action potentials using quantum defects in diamond, *Proc. Natl. Acad. Sci. USA* **113**, 14133 (2016).
- [13] P. Wang, S. Chen, M. Guo, S. Peng, M. Wang, M. Chen, W. Ma, R. Zhang, J. Su, X. Rong, F. Shi, T. Xu, and J. Du, Nanoscale magnetic imaging of ferritins in a single cell, *Sci. Adv.* **5**, eaau8038 (2019).
- [14] A. Zwick, G. A. Álvarez, and G. Kurizki, Maximizing Information on the Environment by Dynamically Controlled Qubit Probes, *Phys. Rev. Appl.* **5**, 014007 (2016).
- [15] A. Zwick, D. Suter, G. Kurizki, and G. A. Álvarez, Precision Limits of Tissue Microstructure Characterization by Magnetic Resonance Imaging, *Phys. Rev. Appl.* **14**, 024088 (2020).
- [16] G. A. Álvarez, N. Shemesh, and L. Frydman, Coherent Dynamical Recoupling of Diffusion-Driven Decoherence in Magnetic Resonance, *Phys. Rev. Lett.* **111**, 080404 (2013).
- [17] G. A. Álvarez, N. Shemesh, and L. Frydman, Diffusion-assisted selective dynamical recoupling: A new approach to measure background gradients in magnetic resonance, *J. Chem. Phys.* **140**, 084205 (2014).
- [18] E. O. Stejskal and J. E. Tanner, Spin diffusion measurements: Spin echoes in the presence of a time-dependent field gradient, *J. Chem. Phys.* **42**, 288 (1965).
- [19] D. S. Grebenkov, NMR survey of reflected Brownian motion, *Rev. Mod. Phys.* **79**, 1077 (2007).
- [20] P. T. Callaghan, *Translational Dynamics and Magnetic Resonance: Principles of Pulsed Gradient Spin Echo NMR* (Oxford University Press, Oxford, 2011).
- [21] J. Stepisnik, Time-dependent self-diffusion by NMR spin-echo, *Phys. B* **183**, 343 (1993).
- [22] N. Shemesh, G. A. Álvarez, and L. Frydman, Measuring small compartment dimensions by probing diffusion dynamics via non-uniform oscillating-gradient spin-echo (NOGSE) NMR, *J. Magn. Reson.* **237**, 49 (2013).
- [23] I. Drobniak, H. Zhang, A. Ianus, E. Kaden, and D. C. Alexander, PGSE, OGSE, and sensitivity to axon diameter in diffusion MRI: Insight from a simulation study, *Magn. Reson. Med.* **75**, 688 (2016).
- [24] M. Nilsson, S. Lasic, I. Drobniak, D. Topgaard, and C.-F. Westin, Resolution limit of cylinder diameter estimation by diffusion MRI: The impact of gradient waveform and orientation dispersion, *NMR Biomed.* **30**, e3711 (2017).
- [25] G. A. Álvarez, N. Shemesh, and L. Frydman, Internal gradient distributions: A susceptibility-derived tensor delivering morphologies by magnetic resonance, *Sci. Rep.* **7**, 3311 (2017).
- [26] D. S. Novikov, E. Fieremans, S. N. Jespersen, and V. G. Kiselev, Quantifying brain microstructure with diffusion MRI: Theory and parameter estimation, *NMR Biomed.* **32**, e3998 (2019).
- [27] S. Lasic, J. Stepisnik, and A. Mohoric, Displacement power spectrum measurement by CPMG in constant gradient, *J. Magn. Reson.* **182**, 208 (2006).
- [28] J. Stepisnik, S. Lasic, A. Mohoric, I. Sersa, and A. Sepe, Spectral characterization of diffusion in porous media by the modulated gradient spin echo with CPMG sequence, *J. Magn. Reson.* **182**, 195 (2006).
- [29] P. T. Callaghan and J. Stepisnik, Frequency-domain analysis of spin motion using modulated-gradient NMR, *J. Magn. Reson.* **117**, 118 (1995).
- [30] E. Hahn, Spin echoes, *Phys. Rev.* **80**, 580 (1950).

- [31] H. Y. Carr and E. M. Purcell, Effects of diffusion on free precession in nuclear magnetic resonance experiments, *Phys. Rev.* **94**, 630 (1954).
- [32] S. Meiboom and D. Gill, Modified spin-echo method for measuring nuclear relaxation times, *Rev. Sci. Instrum.* **29**, 688 (1958).
- [33] D. Suter and G. A. Álvarez, Colloquium: Protecting quantum information against environmental noise, *Rev. Mod. Phys.* **88**, 041001 (2016).
- [34] M. Nilsson, E. Englund, F. Szczepankiewicz, D. van Westen, and P. C. Sundgren, Imaging brain tumour microstructure, *Neuroimage* **182**, 232 (2018).
- [35] D. S. Novikov, V. G. Kiselev, and S. N. Jespersen, On modeling, *Magn. Reson. Med.* **79**, 3172 (2018).
- [36] Y. Assaf, T. Blumenfeld-Katzir, Y. Yovel, and P. J. Basser, Axcaliber: A method for measuring axon diameter distribution from diffusion MRI, *Magn. Reson. Med.* **59**, 1347 (2008).
- [37] N. Shemesh, G. A. Álvarez, and L. Frydman, Size distribution imaging by non-uniform oscillating-gradient spin echo (NOGSE) MRI, *PLoS One* **10**, e0133201 (2015).
- [38] J. Xu, X. Jiang, H. Li, L. R. Arlinghaus, E. T. McKinley, S. P. Devan, B. M. Hardy, J. Xie, H. Kang, A. B. Chakravarthy, and J. C. Gore, Magnetic resonance imaging of mean cell size in human breast tumors, *Magn. Reson. Med.* **83**, 2002 (2020).
- [39] S. Y. Huang, Q. Fan, N. Machado, A. Eloyan, J. D. Bireley, A. W. Russo, S. M. Tobyne, K. R. Patel, K. Brewer, S. F. Rapaport, *et al.*, Corpus callosum axon diameter relates to cognitive impairment in multiple sclerosis, *Ann. Clin. Transl. Neurol.* **6**, 882 (2019).
- [40] J. Veraart, D. Nunes, U. Rudrapatna, E. Fieremans, D. K. Jones, D. S. Novikov, and N. Shemesh, Noninvasive quantification of axon radii using diffusion MRI, *eLife* **9**, e49855 (2020).
- [41] G. S. Uhrig, Keeping a Quantum bit Alive by Optimized π -Pulse Sequences, *Phys. Rev. Lett.* **98**, 100504 (2007).
- [42] E. Jenista, A. Stokes, R. Branca, and W. Warren, Optimized, unequal pulse spacing in multiple echo sequences improves refocusing in magnetic resonance, *J. Chem. Phys.* **131**, 204510 (2009).
- [43] J. R. Klauder and P. W. Anderson, Spectral diffusion decay in spin resonance experiments, *Phys. Rev.* **125**, 912 (1962).
- [44] J. Stepisnik, Validity limits of Gaussian approximation in cumulant expansion for diffusion attenuation of spin echo, *Phys. B* **270**, 110 (1999).
- [45] R. C. Wayne and R. M. Cotts, Nuclear-magnetic-resonance study of self-diffusion in a bounded medium, *Phys. Rev.* **151**, 264 (1966).
- [46] B. Robertson, Spin-echo decay of spins diffusing in a bounded region, *Phys. Rev.* **151**, 273 (1966).
- [47] H. H. Ong and F. W. Wehrli, Quantifying axon diameter and intra-cellular volume fraction in excised mouse spinal cord with q-space imaging, *Neuroimage* **51**, 1360 (2010).
- [48] J. C. Gore, J. Xu, D. C. Colvin, T. E. Yankeelov, E. C. Parsons, and M. D. Does, Characterization of tissue structure at varying length scales using temporal diffusion spectroscopy, *NMR Biomed.* **23**, 745 (2010).
- [49] M. Hurlimann, K. Helmer, T. Deswiet, and P. Sen, Spin echoes in a constant gradient and in the presence of simple restriction, *J. Magn. Reson.* **113**, 260 (1995).
- [50] T. M. de Swiet and P. N. Sen, Decay of nuclear magnetization by bounded diffusion in a constant field gradient, *J. Chem. Phys.* **100**, 5597 (1994).
- [51] D. C. Alexander, P. L. Hubbard, M. G. Hall, E. A. Moore, M. Ptito, G. J. Parker, and T. B. Dyrby, Orientationally invariant indices of axon diameter and density from diffusion MRI, *Neuroimage* **52**, 1374 (2010).
- [52] S. Pajevic and P. J. Basser, An optimum principle predicts the distribution of axon diameters in normal White matter, *PLoS One* **8**, e54095 (2013).
- [53] D. Liewald, R. Miller, N. Logothetis, H.-J. Wagner, and A. Schüz, Distribution of axon diameters in cortical white matter: An electron-microscopic study on three human brains and a macaque, *Biol. Cybern.* **108**, 541 (2014).
- [54] F. Aboitiz, A. B. Scheibel, R. S. Fisher, and E. Zaidel, Fiber composition of the human corpus callosum, *Brain Res.* **598**, 143 (1992).
- [55] R. Caminiti, F. Carducci, C. Piervincenzi, A. Battaglia-Mayer, G. Confalone, F. Visco-Comandini, P. Pantano, and G. M. Innocenti, Diameter, length, speed, and conduction delay of callosal axons in macaque monkeys and humans: Comparing data from histology and magnetic resonance imaging diffusion tractography, *J. Neurosci.* **33**, 14501 (2013).